Materials Research. 2019; 22(suppl. 1): e20180847
DOI: http://dx.doi.org/10.1590/1980-5373-MR-2018-0847

Fe_3O_4@C core-shell nanoparticles as adsorbent of ionic zinc: evaluating of the adsorptive capacity

Tauana Rhodio da Costa[a], Eduarda Baldi[c], Amanda Figueiró[c], Gustavo Lopes Colpani[b], Luciano Luiz Silva[b], Micheli Zanetti[b], Josiane Maria Muneron de Mello[a,b], Márcio Antônio Fiori[a,b]*

[a]Programa de Pós-Graduação em Ciências Ambientais - PPGCA, Área de Ciências Exatas e Ambientais, Universidade Comunitária da Região de Chapecó - Unochapecó, Chapecó, SC, Brasil
[b]Programa de Pós-Graduação em Tecnologia e Gestão da Inovação - PPGTI, Área de Ciências Exatas e Ambientais, Universidade Comunitária da Região de Chapecó - Unochapecó, Chapecó, SC, Brasil
[c]Curso de Graduação em Engenharia Química, Área de Ciências Exatas e Ambientais, Universidade Comunitária da Região de Chapecó - Unochapecó, Chapecó, SC, Brasil

Received: December 17, 2018; Revised: April 14, 2019; Accepted: May 19, 2019

Zinc is an important chemical element in many metabolic mechanisms at low concentrations, but can be toxic when administrated in doses higher than 500 $\mu g \cdot g^{-1}$ or 3 $mg \cdot L^{-1}$. This metal has been detected in many aquatic environments due to several industry activities and swine manure effluents. Thus, the contaminant removal of water and wastewater has been a major challenge. Many processes are applied and evaluated in an attempt to removal zinc found in environment, such as adsorption. In the present study Fe_3O_4@C core-shell nanoparticles were synthesized and used to adsorb ionic zinc species in aqueous solutions. The core-shell nanoparticles exhibited excellent zinc removal capacity, with a maximum efficiency equal 65% where applied in an aqueous solution containing 10 $mg \cdot l^{-1}$ of this ionic metal.

Keywords: *Core-shell nanoparticles, adsorption of zinc, adsorption by magnetite-carbon core-shell nanoparticles.*

1. Introduction

Zinc is a chemical element consider essential for metabolic mechanisms in humans and animals when at low concentrations (<µg)[1,2]. Otherwise, in elevated concentration, upper to 500 $\mu g \cdot g^{-1}$ or 3 $mg \cdot l^{-1}$, zinc can become toxic and cause diarrhea, depression, vomiting, fever, skin irritations, anemia and arteriosclerosis[3-5].

This heavy metal has been detected in several aquatic environments, mainly due to effluents of industrial activities (mining, chemical processes, metallurgy and others), which release zinc into the environment[6,7]. Moreover, this mineral is also found in swine manure wastewater, since it is used in feeds to achieve the optimum growth rate in animals and because of their antimicrobial properties[8]. Meanwhile, approximately 10% of zinc is absorbed by swine organism, and the other part is excreted in the effluent[9].

Therefore, the contaminant removal of aquatic environment has been a difficult challenge. Several processes have been applied and evaluated as an attempt to zinc removal of wastewater and drinking water, such as membrane filtration, ionic change and precipitation process, flotation and reverse osmosis, electrochemical processes, coagulation and adsorption[10,11]. However, these processes show limitations due to technical and economic constraints[12]. In particular, the adsorption process has demonstrated advantageous features, like selectivity, good reproducibility, high efficiency in metal removal, low energy requirements and operational feasibility[13-15].

In this sense, the nanoparticles have been showed high potential to be applied in adsorption. These structures have high surface area that result in an excellent adsorption capacity, with lower mass quantity of adsorbent per effluent volume than other traditional materials[16]. Even with these advantages, discontinuous packed bed removal is still critical in the processes, as well as the recovery of nanoparticles from the aqueous medium is complex[17].

Nanostructured systems with hybrid properties have been studied in order to seek alternatives to apply adsorbent nanoparticles in wastewater treatment with continuous flow, like core-shell nanoparticles of magnetite or hematite.

The nanostructures with a magnetic core, covered by carbon (shell), aggregate the carbon adsorption features, due to chemical affinity, and the magnetic properties of the iron oxide. The combination of both properties in a nanoscale structure allows predicting applications of magnetite core-shell nanoparticles in effluent treatment systems. This method provides a quick and efficient separation of

---

*e-mail: marciofiori@gmail.com.

the nanoparticles dispersed in an effluent[18-21], since after adsorption the core-shell can be removed in a continuous process by the use of magnetic fields outside of pipelines, which are projected to attend this function.

Furthermore, the carbon nanolayers protected the magnetic core against acid and alkaline environments, which can deteriorate the nanostrucuture[22,23]. This carbon shell can also easily functionalized with several chemical groups, like amines, to increase the affinity at metal adsorption[23,24].

The aim of this study was synthesize Fe_3O_4@C core-shell nanoparticles to evaluate the capacity of this adsorbent in removal of ionic zinc species dispersed in aqueous solutions. The results showed that the Fe_3O_4@C nanoparticles have excellent adsorption capacity.

2. Experimental Procedure

2.1 Synthesis of Fe_3O_4@C nanoparticles

The magnetic nanoparticles were synthesized by the hydrothermal co-precipitation method, according Lima et al.[25]. A mass of 11.26 g of glucose (97.5% purity; $C_6H_{12}O_6$; Merck), 37.54 g de urea (99% purity; CH_4N_2O; Vetec) and 15.15 g of iron (III) nitrate (99% purity; $Fe(NO_3)_3 \cdot 9H_2O$; Merck) were dispersed in 250 mL of distilled water. The solution was stirred at room temperature for 15 min to obtain a homogeneous solution. Then, 3.12 g of polyethylene glycol (99% purity; $H(OCH_2CH_2)_nOH$; Dinâmica) was added to above solution, which was stirred again at room temperature for 5 min.

Subsequently, the solution was transferred and then sealed in a 200 mL Teflon-lined stainless-steel (AISI 304) autoclave to avoid gas and/or humity changes with the environment. The reactor was heated at 180 ºC for 18 h in a drying oven (402/3N; Nova Ética).

Afterwards, the solution was transferred to a beaker followed by cooling in room temperature. The resulting solid was washed with distilled water and filtered for three times. Then, the nanoparticles were washed with ethanol (99% purity; C_2H_5OH; Vetec) and filtered for two times. Finally, the nanoparticles were oven dried at 70 ºC for 2 h.

2.2 Characterization of nanoparticles

The crystal structure of synthesized nanoparticles was determined using a X-ray powder diffraction diffractometer (D8, Bruker, USA) using CuKα radiation at tension of 40 kV and current of 40 mA, with 1,5418Å wavelength and in steps of 0.02° (2θ) s^{-1} from 2 to 72° (2θ) at room temperature.

The functional groups at nanoparticles surface were analyzed by Fourier transform infrared (FTIR 4200, Jasco, Japan) spectrophotometer between 4000 and 400 cm^{-1} using the KBr pallet technique.

The specific surface area was determined by Brunauer-Emmett-Teller (BET)[26] analyses, according ASTM D 6556-17[27], and pore volume and diameter were calculated using the Barrett-Johner-Halenda method. Adsorption and desorption isotherms were performed using a static nitrogen adsorption instrument at 77 K (Autosorb 1C, Quantachrome, Austria). The nanoparticles were previously treated at 100 ºC under vacuum (10-7 torr) for 3 h.

The adsorbent morphology and surface elemental composition were determined using a Field Emission Gun Scanning Electron Microscope (SEM-FEG, Tescan, Czech Republic) equipped with an Energy Dispersive Spectrometer (EDS).

2.3 Determination of point of zero charge (pH_{PZC})

The Fe_3O_4@C nanoparticles pH_{PCZ} was measured by modified method described for Babić et al.[28] and Regalbuto and Robles[29]. The experiments were conducted in a series of 125 ml Erlenmeyer flasks containing 50 ml ultrapure water. The initial pH (pHi) in each flask was adjusted approximately between 1 and 12 by adding either 0.1 M HCl (99% purity; Vetec) or 0.1 M NaOH (99% purity; Vetec), using pH meter (W3B, Bel Engineering®). 0.1 g of adsorbent was added to all 12 flasks and they were placed on shaker (LS 4500, Logen Scientific, UK) at 120 rpm and 25 ºC for 24h. Subsequently, the samples were filtrated through syringe Durapore® (Cork, IE) PVDF membranes, with diameter pores of 0.22 µm and and the pH final values (pHfinal) were measured again. Intersection point of the resulting curve with the line passing origin ($pH_{final}=pH_{initial}$) gives pH_{PZC}[30].

2.4 Adsorption kinetics

The adsorption kinetics were performed in 250 ml Erlenmeyers flasks under batch conditions. 0.5 g of Fe_3O_4@C nanoparticles was added in 100 ml aqueous solution containing 10 ppm of ionic zinc species. The samples were placed on shaker (LS 4500, Logen Scientific, UK) at 140 rpm and 25 ºC. During experiments, pH was kept equal 5.5. Aliquots of adsorption media were removed at regular time periods centrifuged (Excelsea II 260BL, Fanem, Brazil) (3400 rpm for 10 min) and filtrated through PVDF membranes with diameter pores of 0.22 µm. The zinc concentration was estimated by Atomic Absorption Spectrophotometer (Analyst 800 AAS, Perkin Elmer, USA). All experiments were done in triplicates.

The adsorption capacity is calculated using Eq. (1).

$$q_e = V\frac{(C_o - C_e)}{m} \tag{1}$$

where q_e ($mg \cdot g^{-1}$) is the adsorption capacity at the equilibrium; C_0 and C_e ($mg \cdot l^{-1}$) are the initial and equilibrium concentrations of solution, respectively; V (l) is the volume of the aqueous solution and m (g) is the mass of adsorbent used in the experiments.

The adsorption capacities were related with kinetic times and evaluated for three adsorption kinetic models. The pseudo-first order model, the pseudo-second order model and the intra-particle diffusion model, were applied to interpreting the experiment data. The equations of the models are described as follows:

Pseudo-first order kinetic:

$$\frac{dq_t}{dt} = k_1\left(q_e - q_t\right) \tag{2}$$

Pseudo-second order kinetic:

$$\frac{dq_t}{dt} = k_2\left(q_e - q_t\right)^2 \tag{3}$$

Intraparticle diffusion kinetic:

$$q_t = k_{in}.t^{\frac{1}{2}} + C \tag{4}$$

where k_1 (min^{-1}) is the first-order rate constant; k_2 ($mg \cdot g^{-1} \cdot min^{-1}$) is the second-order rate constant; k_{in} ($mg \cdot g^{-1} \cdot min^{-1/2}$) is the intraparticle diffusion rate constant; C ($mg \cdot g^{-1}$) is a constant related to the diffusion resistance. q_e and q_t ($mg \cdot g^{-1}$) are the amount of zinc adsorbed at the equilibrium and at time t (min), respectively.

The kinetic parameters of the models evaluated are determined using Statistica® 7.0 (StatSoft®, USA). The Quasi-Newton method was applied to minimize the square sum of errors (SSE), which is calculated using Eq. (5). q_{exp} and q_{cal} are the experimental and calculated adsorption capacity, respectively.

$$SSE = \sum_i^p \left(q_{\exp} - q_{cal}\right) \tag{5}$$

2.5 Adsorption isotherms

The batch adsorption isotherms experiments were carried out by adding different adsorbent mass (0.1 to 0.9 g) into 100 mL of aqueous solutions with an ionic zinc concentration equal 10 ppm. pH of all solutions was adjusted at 5.5 using 0.1 M HCl. Solutions were agitated in shaker at 140 rpm and 25 ºC for 24 h. After experimental procedure, aliquots of adsorption media were removed, centrifuged (Excelsea II 260BL, Fanem, Brazil) (3400 rpm for 10 min) and filtrated through PVDF membranes with diameter pores of 0.22 µm. The zinc concentration was estimated by Atomic Absorption Spectrophotometer (Analyst 800 AAS, Perkin Elmer, USA). All experiments were done in triplicates. In order to describe the interactive behavior between solute and adsorbent, the Langmuir, Freundlich and Langmuir-Freundlich models were applied to analyze the adsorption data. The equations of the models are described as follows:

Langmuir isotherm:

$$q_e = \frac{q_{\max} b_L C_e}{1 + b_L C_e} \tag{6}$$

Freundlich isotherm:

$$q_e = k_F C_e^{1/n} \tag{7}$$

Langmuir-Freundlich isotherm:

$$q_e = \frac{q_{\max}\left(b_{LF} C_e\right)^m}{1 + \left(b_{LF} C_e\right)^m} \tag{8}$$

where q_e and q_{max} are the amount of zinc adsorbed at equilibrium and at saturation, respectively, ($mg \cdot g^{-1}$); C_e is the concentration of zinc in the liquid phase at equilibrium ($mg \cdot l^{-1}$); b_L is the Langmuir adsorption equilibrium that represents surface affinity ($l \cdot mg^{-1}$). k_f is Freundlich constant and $1/n_f$ is the adsorption intensity. m_{LF} is the Langmuir-Freundlich constant and b_{LF} is the affinity parameter ($l \cdot mg^{-1}$).

3. Results and Discussion

3.1 Characterization of nanoparticles

The morphology of the Fe_3O_4@C nanoparticles was evaluated by SEM method. Figure 1 depicts SEM-FEG micrographs and reveals that nanoestructures show spherical geometry, with diameters near 20 nm, which form irregular agglomerates with diameters from 100 to 300 nm. This agglomerate formation indicates that the surface energy of the nanoparticles is relatively strong. Similar results are obtained by Huong et al.[22] and Ye et al.[31].

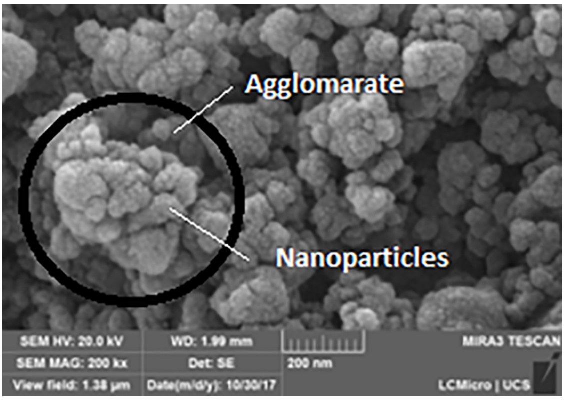

Figure 1. SEM image of Fe_3O_4@C core-shell nanoparticles.

The elemental maps are shown in Figure 2. These analyses are performed with EDS and clearly showed the uniform distribution of Fe, O and C elements in the structure of Fe_3O_4@C nanoparticles. The iron and oxygen presence is related with iron oxide core. Carbon was also verified in the scanning and its presence is consistent with the carbon nanolayer (shell). The EDS results are similar that obtained by Huang et al.[32] and Li et al.[33].

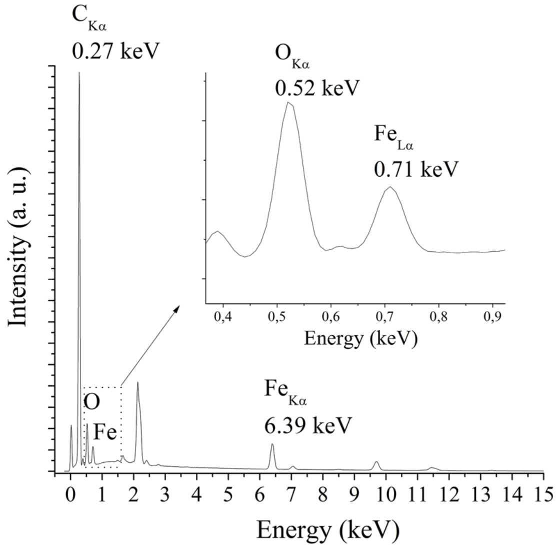

Figure 2. EDS pattern of Fe_3O_4@C nanoparticles.

Figure 3 demonstrated a micrograph performed by SEM-FEG and the chemical distribution obtained to Fe, O and C by x-ray fluorescence. Figure 3(a) confirms the agglomerate formation with dimensions near 100 nm to 300 nm and Figures 3(b), 3(c) and 3(d) depict the presence of iron, oxygen and carbon elements, respectively.

Figure 4 shows the diffraction patterns of the as-prepared samples. The peaks detected at 24.3°, 33.3°, 35.7°, 40.9°, 49.5°, 54.2°, 57.6°, 62.5° and 64.1° corresponding, respectively, to the crystal planes [012], [104], [110], [113], [024], [116], [122], [214] and [300] da α-hematite[34-36].

However, when nanoparticles are formed in the presence of glucose, to obtain the core-shell, there is the production of magnetite nanoparticles, such as depicted in the XRD demonstrated in Figure 4, where the diffraction peaks at 18.3°, 30.1°, 35.4°, 37.0°, 43.0°, 53.4°, 56.9° and 62.5° can be assigned to the [111], [220], [311], [222], [400], [422], [511] and [440] crystal planes of Fe_3O_4[37-40], according the Crystallography Open Database (Fe_3O_4 - COD 96-900-9770). It is possible that the oxygen released by glucose during the formation of the carbon nanolayer reacted with hematite, which was oxidized to magnetite. The peak inherent to carbon ($2\theta \approx 26°$)[40], according the Crystallography Open Database (Carbon - COD 96-120-0018), was not distinguished at diffractogram, possibly duo to low concentration in relation to Fe_3O_4 core of the nanoparticles.

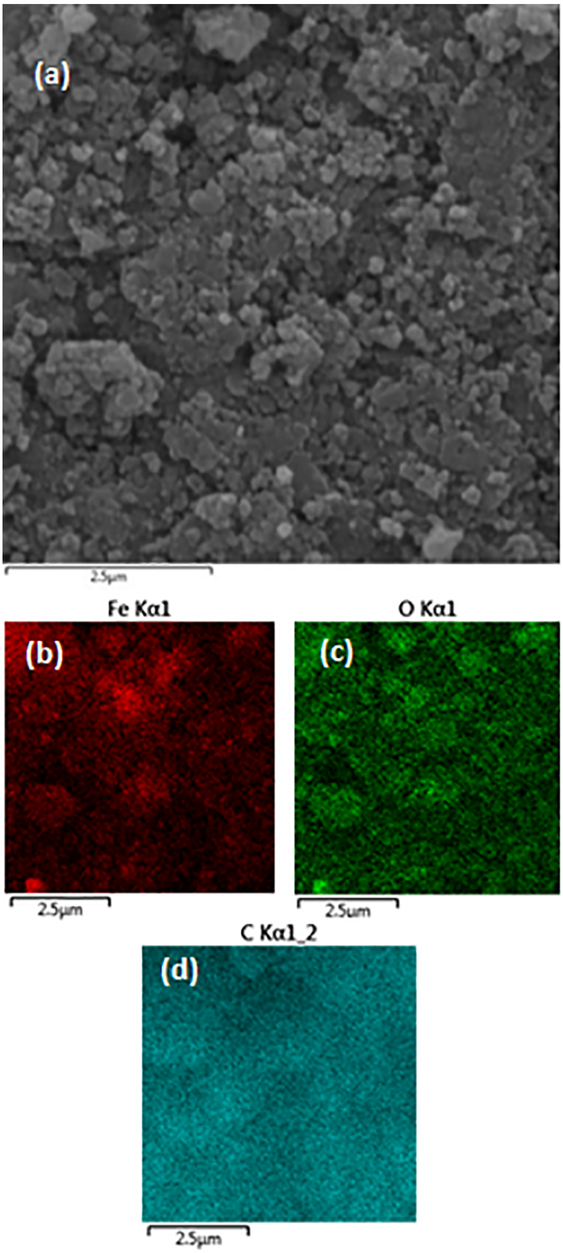

Figure 3. (a) SEM-FEG micrograph of Fe_3O_4@C nanoparticles. (b) Elemental map distribution of (b) iron, (c) oxygen and (d) carbon.

As shown in Table 1, the Rietveld refinement exhibit the presence of carbon and iron, with a higher content of the inorganic element in relation to carbon, as expected due to the organic element to be content only at the surface. The unit cell parameters of each element are similar to that reported at literature[41]. The carbon exhibit detected in the core-shell nanoparticles has orthorhombic crystalline structure and the iron oxide possess a cubic unit cell.

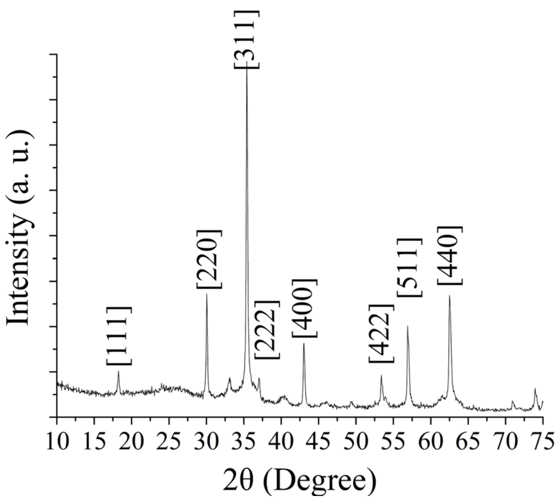

Figure 4. XRD pattern of Fe_3O_4@C and Fe_2O_3 core-shell nanoparticles. Crystallography Open Database: Fe_3O_4 - COD 96-900-9770 and Carbon - COD 96-120-0018.

The Scherrer method was applied with $k = 0.94$ (considering spherical crystallite) to determine the crystallite of the core-shell nanoparticles. The crystal sizes values, determined by Rietveld method, are similar to the average size of the nanoparticles observed by SEM, which confirms that the nanoparticles do not possess significant crystal defects.

The crystal size difference between core-shell nanoparticles and hematite could be related to the presence of carbon nanolayer, since this structure covers the core.

FT-IR spectra was obtained to evaluate the presence of functional groups in the nanoparticles assigned to the magnetite and carbon in the core-shell nanoparticles. Figure 5 depicts a peak at 582 cm^{-1} wavenumber, which identify the Fe-O vibrational bond[42] and confirm the Fe_3O_4 presence in these nanoparticles. The peak at 1580 cm^{-1} is reasonably assingned to the C=C[43] stretching vibration. This peak indicates the presence of carbon at the nanostructure. Moreover, two bands located at 2850 cm^{-1} and 2920 cm^{-1} could be attributed to C-H stretching vibration[24].

A wide vibration around 3000-3500 cm^{-1} correspond to the stretching vibrations of hydroxyl groups or hydrogen bonded molecular water species, probably adsorbed at the surface of Fe_3O_4@C nanoparticles.

As shown in Table 2, the surface area, pore size and pore volume of Fe_3O_4@C nanoparticles were obtained using BET e BJH models. The core-shell have a mesoporous structure according the models, with pore diameter mean of 16 nm. However, this pore size probably is attributed to the porosity formed into nanoparticles interfaces that constitute the agglomerates.

The specific surface area is equal 63.56 $m^2 \cdot g^{-1}$ and this result is near to the obtained by Strachowski and Bystrzejewski[19] and Konicki et al.[23]. This value probably is related to the mean specific surface area of the agglomerates formed by Fe_3O_4@C nanoparticles, since these nanostructures have a reduced porosity.

3.2 Point of zero charge

Figure 6 depicts the point of zero charge (pH_{PZC}) of Fe_3O_4@C nanoparticles. The pH_{PZC} corresponds to the range in which the final pH remains constant regardless of initial pH. The value where the net surface charge on the core-shell nanoparticles remains zero in an electrolyte solution was found at approximately 5.0. Then, at a $pH < pH_{PZC}$ the surface of the adsorbent is positively charged and preferentially adsorbs anions. For the $pH > pH_{PZC}$, the surface of nanoparticles contains negative charges and attracts cations[44].

Therefore, the Zn^{2+} ionic species adsorption at Fe_3O_4@C nanoparticles will be improved in aqueous solutions with pH above 5.0.

3.3 Adsorption kinetics

As shown in Figure 7, the adsorption capacity was evaluated using normalized concentrations values of the ionic zinc during 120 min.

The results indicate that zinc concentration was reduced significantly to 64% at 10 min. This distinguished reduction possibly is due to concentration gradient of the adsorbate in the adsorbent and the aqueous solutions. Moreover, this kinetic response can be associated to the adsorption of the zinc ionic species on the external surface, which occurs with reduced resistance. However, the mechanism changes after 10 min probably occurs because the intraparticle diffusion, which increases the resistance[45,46]. But, the presence of the agglomerates of Fe_2O_3 core-shell can to prejudice or even prevent the rapid adsorption after this time and contribute to the decreases the adsorption rate of the zinc specimens.

The diffusion mechanism in the adsorption process initially is quick and occurs mostly in the boundary layer, between the aqueous solution and adsorbate. Following this mechanism there is the solute diffusion inside the pores and in the capillaries of the Fe_3O_4@C nanoparticles. This high adsorption efficiency can be ascribed to abundant unoccupied

Table 1. Results of Rietveld analysis for the Fe_3O_4@C nanoparticles. XRD pattern: monocristaline silicon.

Sample	Phase	Content (wt%)	Unit cell Parameters (Å)	Particle size (nm)	X^2
Fe_3O_4@C	C	7.6	a=b=2.47 c= 6.79	71.34	4.8
	Fe_3O_4	92.4	a=b=c= 8.38		

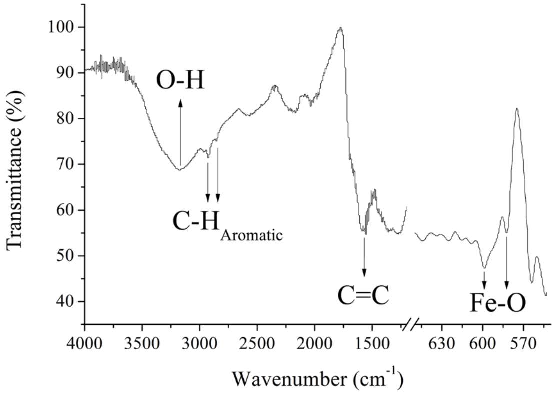

Figure 5. FTIR spectra for the Fe_3O_4@C nanoparticles.

Table 2. BET and BJH surface parameters of Fe_3O_4@C nanoparticles.

Sample	Surface area ($m^2 \cdot g^{-1}$)	Pore size (nm)	Pore volume ($cm^3 \cdot g^{-1}$)
Fe_3O_4@C	63.56	16.07	0.18

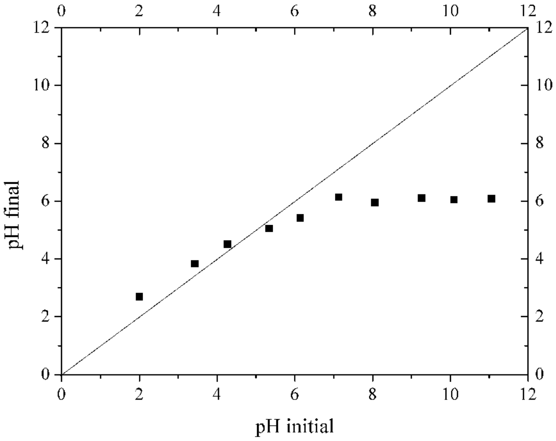

Figure 6. pH at the point of zero charge of Fe_3O_4@C nanoparticles at 25 °C.

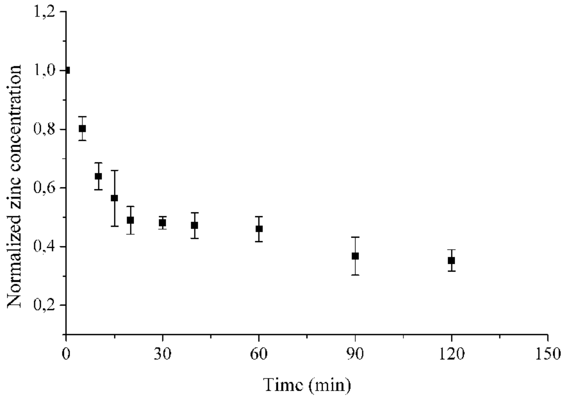

Figure 7. Zinc ionic species removal using Fe_3O_4@C nanoparticles in aqueous solutions (Temperature = 25°C, pH = 5.5 $[Zn^{2+}]_0$ = 10 mg·$^{-1}$, [Fe_3O_4@C] = 5 mg·ml^{-1}).

active sites on the surface of the adsorbent and high zinc concentration gradient at the initial stage[15].

The results indicate that the kinetic equilibrium condition for the adsorption process of the zinc specimens can be obtained in times close to 120 min, with a zinc removal capacity near 65%. The mechanisms involved in the adsorption process were evaluated adjusting the experimental data with the kinetic models of pseudo-first order model, the pseudo-second order model and the intraparticle diffusion model, as shown in Figures 8 and 9.

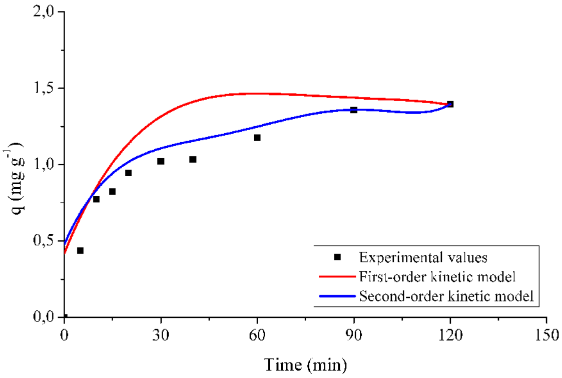

Figure 8. Adsorption kinetics of Zn^{2+} on Fe_3O_4@C nanoparticles fitted by pseudo-first order and pseudo-second order.

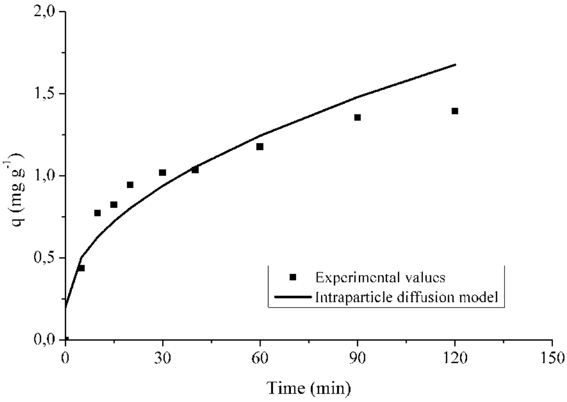

Figure 9. Adsorption kinetics of Zn^{2+} on Fe_3O_4@C nanoparticles fitted by intraparticle diffusion model.

The model parameters and the quality of the fitting were adjusted in terms of correlation coefficient (R^2) for each model. The values of the correlation coefficients were compared with each other, and the higher value was considered the better adjustment. Furthermore, the experimental adsorption capacity in the equilibrium (qe_{exp}) was compared with the calculated parameter (qe_{calc}) obtained with the kinetic adsorption models. The kinetic models are significant when the difference between experimental and calculated adsorption capacity is the smallest possible.

The values for the kinetic adsorption constants are shown in Tables 3 and 4. These values were determined from the application of the pseudo-first order, pseudo-second order and intraparticle diffusion models for the amount of solute adsorbed per gram of the adsorbent, under equilibrium conditions.

Table 3. Kinetic parameters of zinc adsorption.

	Pseudo-first order	Pseudo-second order	Intraparticle diffusion
k_1(min^{-1})	0.052	-	-
k_2(min^{-1})	-	0.050	-
C (mg·g^{-1})	-	-	0.135
k_{in}(mg·g^{-1}·min$^{-1/2}$)	-	-	0.200
R^2	**0.882**	**0.952**	**0.954**

Table 4. Parameters of adsorption capacity for zinc removal.

Kinetic Model	$q_{e\,(exp)}$ (mg·g^{-1})	$q_{e\,(calc)}$ (mg·g^{-1})	Deviation (%)	R^2
Pseudo-first order	1.394	1.292	7.320	0.952
Pseudo-second order	1.394	1.406	0.860	0.954

The kinetics parameters obtained by fitting the experimental data demonstrated that the pseudo-second order and intraparticle diffusion precisaly describe the adsorption mechanism.

The pseudo-second order predicts the adsorption behavior during all the process and it defines that occurs chemisorption with formation of complexes or functional groups, due to ionic pairing. According to Colpani[47], in the chemisorption there is the formation of a adsorbate monolayer chemically bound to the surface of the nanoparticles, which is followed by additional layers, physically bound, of the adsorbed compound. This chemical bond probably will make it impossible to reuse the core-shell. Huo et al.[42] evaluated an anionic dye adsorption using magnetic Fe_3O_4 and copolymer modified Fe_3O_4 nanostructures. The kinetics adsorption fitting to pseudo-second order model. Shan et al.[48] used Fe_3O_4 nanoparticles to mercury removal and the results also indicate a good linear fit for the pseudo-second order model.

As depicted in Figure 9 and Table 3, the intraparticle diffusion model also can predict the experimental results quite well, since it had a satisfactory adjustment. Nevertheless, it is possible to verify that the nonlinear regression fitting to the analyzed data does not intercept the origin and C value is not zero, representing a multi-linear process with contributions from the other mechanisms as well[49-50]. Thus, the intraparticle diffusion mechanism is not the main process in the adsorption kinetic and mass transfer. Lima et al.[51] evaluated the nitrate, sulfate and phosphate removal by green coconut shell fibers adsorbent modified with ammonium quaternary salt. In this case, the results also were fitted to the intraparticle diffusion and the linear line does not pass through the origin. These deviations from the origin probably are related to the difference in the mass transfer rate in the initial and final stages of adsorption, which means that the pore diffusion is not the limiting stage of the adsorptive process. Moreover, the low value of C parameter indicates that the effect of boundary layer is reduced[52].

3.4 Adsorption isotherms

The Langmuir, Freundlich and Langmuir-Freundlich models were used to find out the accurate adsorption model that representing the experimental data and for predicting the mechanisms of core-shell nanoparticles. As shown in Figure 10, the experimental data were fitted to the above mentioned isotherm models and the parameters of the isotherms data are listed in Table 5.

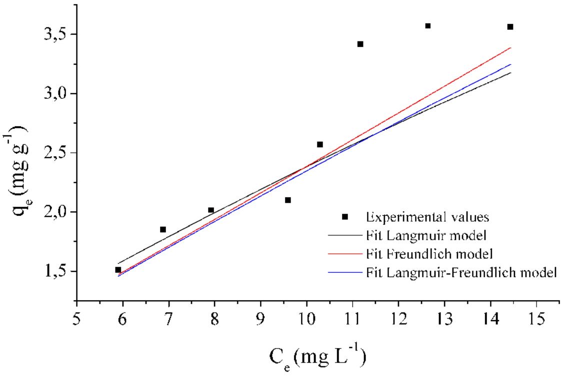

Figure 10. Equilibrium adsorption isotherms for zinc removal fitted to Langmuir, Freundlich and Langmuir-Freundlich.

The R^2 values suggested that Langmuir-Freundlich fitted the data most than other Langmuir and Freundlich, but with a small difference between the isotherms models.

The Langmuir-Freundlich isotherm has been applied to analyze the adsorption in heterogeneous surface, with a exponential relation between the adsorbate disperse in aqueous solution and bound in the adsorbent[53,54]. This model follows the Freundlich model when the concentration of the adsorbate is low, which leads to the hyphotesis of multilayer adsorption. On the other hand, for high concentration of the adsorbate, this model is more similar to the Langmuir isotherm that describes the chemisorption and monolayer coverage until saturation. The value of m_{LF} in Table 5 is equals 1.464. When this parameter is higher than 1.0 the adsorption is favored, without saturation of the core-shell nanoparticles surface[55].

The goodness-of-fit of Langmuir-Freundlich indicates that the Fe_3O_4@C nanoparticles have heterogeneous surface sites, suggesting that the adsorption of zinc ionic species were likely to take place by the formation of multilayer coverage on the energetically heterogeneous.

Table 5. Equilibrium parameters for the adsorption of Zn^{2+} ionic species onto Fe_3O_4@C nanoparticles.

Langmuir		Freundlich		Langmuir-Freundlich	
q_{max} (mg·g^{-1})	20.010	n_f	0.242	q_{mLF} (mg·g^{-1})	9.151
b_L (l·mg^{-1})	0.025	k_f	0.968	b_{LF} (l·mg^{-1})	0.054
R_L	0.787			m_{LF}	1.464
R^2	0.878	R^2	0.887	R^2	0.891

Oyetade et al.[56] evaluated the adsorption capacity of functionalized multiwalled carbon nanotubes for the removal of lead and zinc ions from aqueous solution. The maximum adsorption capacity (q_{mLF}) and affinity parameter (b_{LF}) obtained to the Langmuir-Freundlich model were equal 18.52 mg·g^{-1} and 0.037 l·mg^{-1}. Vázquez et al.[57] investigated the potential of chestnut shell waste in Zn^{2+} removal from aqueous solutions. In this study the Langmuir-Freundlich also isotherm fitted better Zn^{2+} experimental data, with q_{mLF} equal 8.88 mg·g^{-1}. It is possible to perceive that the best isotherm model to describe the adsorption equilibrium for the range of initial cation concentration studied was the Langmuir-Freundlich model.

4. Conclusion

The nanoparticles characterizations demonstrated that the hydrothermal co-precipitation method successfully formed Fe_3O_4@C core-shell, with a carbon nanolayer that covers a magnetite core. The nanostructures show spherical geometry with dimensions near 20 nm and they have a tendency to form agglomerates.

The zinc removal by Fe_3O_4@C core-shell reached an adsorption capacity approximately equal 65% when applied aqueous solutions containing 10 mg·l^{-1} of ionic zinc and 5 mg·ml^{-1} of adsorbent.

The kinetics study showed that the pseudo-second order model was the best model that comfortably fitted the experimental data, with an adsorption capacity at the equilibrium equal 1.406 mg·g^{-1}. The experimental isotherm data fitted well onto the Langmuir-Freundlich model with the maximum amount of Zn^{2+} being adsorbed at pH 5.5.

5. Acknowledgment

The authors are grateful to the UNOCHAPECÓ and CAPES for the financial support and availability of the infrastructure during the research.

6. References

1. Zhang C, Yu K, Li F, Xiang J. Acute toxic effects of zinc and mercury on survival, standard metabolism, and metal accumulation in juvenile ridgetail white prawn, *Exopalaemon carinicauda. Ecotoxicology and Environmental Safety*. 2017;145:549-556.
2. Alebrahim MF, Khattab IA, Cai Q, Sanduk M. Practical study on the electrochemical simultaneous removal of copper and zinc from simulated binary-metallic industrial wastewater using a packed-bed cathode. *Egyptian Journal of Petroleum*. 2017;26(2):225-234.
3. Ngabura M, Hussain SA, Ghani WAWA, Jami MS, Tan YP. Utilization of renewable durian peels for biosorption of zinc from wastewater. *Journal of Environmental Chemical Engineering*. 2018;6(2):2528-2539.
4. Benali I, Boutiba Z, Grandjean D, de Alencastro LF, Rouane-Hacene O, Chèvre N. Spatial distribution and biological effects of trace metals (Cu, Zn, Pb, Cd) and organic micropollutants (PCBs, PAHs) in mussels *Mytilus galloprovincialis* along the Algerian west coast. *Marine Pollution Bulletin*. 2017;115(1-2):539-550.
5. Carolin CF, Kumar PS, Saravanan A, Joshiba GJ, Naushad M. Efficient techniques for the removal of toxic heavy metals from aquatic environment: A review. *Journal of Environmental Chemical Engineering*. 2017;5(3):2782-2799.
6. Kishimoto N, Narazaki Y, Takemoto K. Reusability of zero-valent iron particles for zinc ion separation. *Separation and Purification Technology*. 2018;193:139-146.
7. Petcu C, Purcar V, Radu AL, Raluca I, Alexandrescu E, Sarbu A, et al. Removal of zinc ions from model wastewater system using bicopolymer membranes with fumed silica. *Journal of Water Process Engineering*. 2015;8:1-10.
8. Zhang R, Wang X, Gu J, Zhang Y. Influence of zinc on biogas production and antibiotic resistance gene profiles during anaerobic digestion of swine manure. *Bioresource Technology*. 2017;244(Pt 1):63-70.
9. Zhou Q, Lin Y, Li X, Yang C, Han Z, Zeng G, et al. Effect of zinc ions on nutrient removal and growth of *Lemna aequinoctialis* from anaerobically digested swine wastewater. *Bioresource Technology*. 2018;249:457-463.

10. Siyal AA, Shamsuddin MR, Khan MI, Rabat NE, Zulfiqar M, Man Z, et al. A review on geopolymers as emerging materials for the adsorption of heavy metals and dyes. *Journal of Environmental Management*. 2018;224:327-339.
11. Burakov AE, Galunin EV, Burakova IV, Kucherova AE, Agarwal S, Tkachev AG, et al. Adsorption of heavy metals on conventional and nanostructured materials for wastewater treatment purposes: A review. *Ecotoxicology and Environmental Safety*. 2018;148:702-712.
12. Sherlala AIA, Raman AAA, Bello MM, Asghar A. A review of the applications of organo-functionalized magnetic graphene oxide nanocomposites for heavy metal adsorption. *Chemosphere*. 2018;193:1004-1017.
13. Da'na E. Adsorption of heavy metals on functionalized-mesoporous silica: A review. *Microporous and Mesoporous Materials*. 2017;247:145-157.
14. Peng W, Li H, Liu Y, Song S. A review on heavy metal ions adsorption from water by graphene oxide and its composites. *Journal of Molecular Liquids*. 2017;230:496-504.
15. Lv Y, Li P, Che Y, Hu C, Ran S, Shi P, et al. Facile Preparation and Characterization of Nanostructured BiOI microspheres with certain adsorption-photocatalytic properties. *Materials Research*. 2018;21(3):e20170705.
16. El-Lateef HMA, Ali MMK, Saleh MM. Adsorption and removal of cationic and anionic surfactants using zero-valent iron nanoparticles. *Journal of Molecular Liquids*. 2018;268:497-505.
17. Ashrafi A, Rahbar-Kelishami A, Shayesteh H. Highly efficient simultaneous ultrasonic assisted adsorption of Pb (II) by Fe_3O_4@MnO_2 core-shell magnetic nanoparticles: Synthesis and characterization, kinetic, equilibrium, and thermodynamic studies. *Journal of Molecular Structure*. 2017;1147:40-47.
18. Shi D, Yang H, Ji S, Jiang S, Liu X, Zhang D. Preparation and Characterization Of Core-Shell Structure Fe_3O_4@C Magnetic Nanoparticles. *Procedia Engineering*. 2015;102:1555-1562.
19. Strachowski P, Bystrzejewski M. Comparative studies of sorption of phenolic compounds onto carbon-encapsulated iron nanoparticles, carbon nanotubes and activated carbon. *Colloids and Surfaces A: Physicochemical and Engineering Aspects*. 2015;467:113-123.
20. Lobato NCC, Mansur MB, Ferreira AM. Characterization and Chemical Stability of Hydrophilic and Hydrophobic Magnetic Nanoparticles. *Materials Research*. 2017;20(3):736-746.
21. Salviano LB, Cardoso TMS, Silva GC, Dantas MSS, Ferreira AM. Microstructural Assessment of Magnetite Nanoparticles (Fe_3O_4) Obtained by Chemical Precipitation Under Different Synthesis Conditions. *Materials Research*. 2018;21(2):e20170764.
22. Huong PTL, Huy LT, Lan H, Thang LH, An TT, Quy NV, et al. Magnetic iron oxide-carbon nanocomposites: Impacts of carbon coating on the As(V) adsorption and inductive heating responses. *Journal of Alloys and Compounds*. 2018;739:139-148.
23. Konicki W, Hełminiak A, Arabczyk W, Mijowska E. Adsorption of cationic dyes onto Fe@graphite core-shell magnetic nanocomposite: Equilibrium, kinetics and thermodynamics. *Chemical Engineering Research and Design*. 2018;129:259-270.
24. Jin S, Park BC, Ham WS, Pan L, Kim YK. Effect of the magnetic core size of amino-functionalized Fe_3O_4 mesoporous SiO_2 core-shell nanoparticles on the removal of heavy metal ions. *Colloids and Surfaces A: Physicochemical and Engineering Aspects*. 2017;531:133-140.
25. Lima MM, Gonçalves JPZ, Soares C, Riella HG, Fernandes SC, Fiori MA, et al. Iron-Carbon Core-Shell Nanoparticles Obtained with Different Conditions of Synthesis. *Materials Science Forum*. 2017;899:221-226.
26. Brunauer S, Emmett PH, Teller E. Adsorption of Gases in Multimolecular Layers. *Journal of the American Chemical Society*. 1938;60(2):309-319.
27. ASTM International. *ASTM- D-6556-17 - Standard Test Method for Carbon Black-Total and External Surface Area by Nitrogen Adsorption*. West Conshohocken: ASTM International; 2017.
28. Babić BM, Milonjić SK, Polovina MJ, Kaludierović BV. Point of zero charge and intrinsic equilibrium constants of activated carbon cloth. *Carbon*. 1999;37(3):477-481.
29. Regalbuto JR, Robles J. *The Engineering of Pt/Carbon Catalyst Preparation For application on Proton Exchange Fuel Cell Membrane (PEFCM)*. Chicago: University of Illinois; 2004. Available from: https://amrel.bioe.uic.edu/NSFREU2004/Reports2004/Jaime%20Robles_Final%20Report.pdf
30. Bayazit ŞS, Kerkez Ö. Hexavalent chromium adsorption on superparamagnetic multi-wall carbon nanotubes and activated carbon composites. *Chemical Engineering Research and Design*. 2014;92(11):2725-2733.
31. Ye Y, Zhang H, Chen Y, Deng P, Huang Z, Liu L, et al. Core-shell structure carbon coated ferric oxide (Fe_2O_3@C) nanoparticles for supercapacitors with superior electrochemical performance. *Journal of Alloys and Compounds*. 2015;639:422-427.
32. Huang J, Li Y, Jia X, Song H. Preparation and tribological properties of core-shell Fe_3O_4@C microspheres. *Tribology International*. 2019;129:427-435.
33. Li Q, Tang G, Xiong S, Cao Y, Chen L, Xu F, et al. Carbon coated magnetite nanoparticles with improved water-dispersion and peroxidase-like activity for colorimetric sensing of glucose. *Sensors and Actuators B: Chemical*. 2015;215:86-92.
34. Basu P, Bhanja P, Salam N, Dey TK, Bhaumik A, Das D, et al. Silver nanoparticles supported over Al_2O_3@Fe_2O_3 core-shell nanoparticles as an efficient catalyst for one-pot synthesis of 1,2,3-triazoles and acylation of benzyl alcohol. *Molecular Catalysis*. 2017;439:31-40.
35. Fu H, Sun S, Yang X, Li W, An X, Zhang H, et al. A facile coating method to construct uniform porous α-Fe_2O_3@TiO_2 core shell nanostructures with enhanced solar light photocatalytic activity. *Powder Technology*. 2018;328:389-396.

36. Cheng Y, Guo Y, Zhang Z, Dong S, Liu S, Wang H. Achieving the broader frequency electromagnetic absorber by development of magnetic core-shell composite with tunable shell/core sizes. *Applied Surface Science*. 2018;434:763-770.

37. Leostean C, Pana O, Stefan M, Popa A, Toloman D, Senila M, et al. New properties of Fe_3O_4@SnO_2 core shell nanoparticles following interface charge/spin transfer. *Applied Surface Science*. 2018;427(Pt A):192-201.

38. Madhubala V, Kalaivani T. Phyto and hydrothermal synthesis of Fe_3O_4@ZnO core-shell nanoparticles using *Azadirachta indica* and its cytotoxicity studies. *Applied Surface Science*. 2018;449:584-590.

39. Wan X, Zhan Y, Long Z, Zeng G, He Y. Core@double-shell structured magnetic halloysite nanotube nano-hybrid as efficient recyclable adsorbent for methylene blue removal. *Chemical Engineering Journal*. 2017;330:491-504.

40. Cheng Y, Zhao H, Yang Z, Lv J, Cao J, Qi X, et al. An unusual route to grow carbon shell on Fe_3O_4 microspheres with enhanced microwave absorption. *Journal of Alloys and Compounds*. 2018;762:463-472.

41. Vezzù K, Delpeuch AB, Negro E, Polizzi S, Nawn G, Bertasi F, et al. Fe-carbon nitride "*Core-shell*" electrocatalysts for the oxygen reduction reaction. *Electrochimica Acta*. 2016;222:1778-1791.

42. Huo Y, Wu H, Wang Z, Wang F, Liu Y, Feng Y, et al. Preparation of core/shell nanocomposite adsorbents based on amine polymer-modified magnetic materials for the efficient adsorption of anionic dyes. *Colloids and Surfaces A: Physicochemical and Engineering Aspects*. 2018;549:174-183.

43. Shah MT, Alveroglu E. Synthesis and characterization of magnetite nanoparticles having different cover layer and investigation of cover layer effect on the adsorption of lysozyme and bovine serum albumin. *Materials Science & Engineering: C*. 2017;81:393-399.

44. Čerović LS, Milonjić SK, Todorović MB, Trtanj MI, Pogozhev YS, Blagoveschenskii Y, et al. Point of zero charge of different carbides. *Colloids and Surfaces A: Physicochemical and Engineering Aspects*. 2007;297(1-3):1-6.

45. Vidal CB, Raulino GSC, Barros AL, Lima ACA, Ribeiro JP, Pires MJR, et al. BTEX removal from aqueous solutions by HDTMA-modified Y zeolite. *Journal of Environmental Management*. 2012;112:178-185.

46. Orlandi G, Cavasotto J, Machado Junior FRS, Colpani GL, Dal Magro J, Dalcanton F, et al. An adsorbent with a high adsorption capacity obtained from the cellulose sludge of industrial residues. *Chemosphere (Oxford)*. 2017;169:171-180.

47. Colpani GL. *Preparação e caracterização de adsorventes para a remoção de surfactantes aniônicos em águas residuárias*. [Dissertation]. Florianópolis: Federal University of Santa Catarina, Chemical and Food Engineering Department; 2012.

48. Shan C, Ma Z, Tong M, Ni J. Removal of Hg(II) by poly(1-vinylimidazole)-grafted Fe_3O_4@SiO_2 magnetic nanoparticles. *Water Research*. 2015;69:252-260.

49. Weber WJ, Morris JC. Kinetics of Adsorption on Carbon from Solution. *Journal of the Sanitary Engineering Division American Society*. 1963;89(2):31-60.

50. da Rocha ORS, do Nascimento GE, Campos NF, da Silva VL, Duarte MMMB. Avaliação do processo adsortivo utilizando mesocarpo de coco verde para remoção do corante cinza reativo BF-2R. *Química Nova*. 2012;35(7):1369-1374.

51. de Lima ACA, Nascimento RF, de Sousa FF, Mendes-Filho J, Oliveira AC. Modified coconut shell fibers: A green and economical sorbent for the removal of anions from aqueous solutions. *Chemical Engineering Journal*. 2012;185-186:274-284.

52. Dizge N, Aydiner C, Demirbas E, Kobya M, Kara S. Adsorption of reactive dyes from aqueous solutions by fly ash: Kinetic and equilibrium studies. *Journal of Hazardous Materials*. 2008;150(3):737-746.

53. Derylo-Marczewska A, Jaroniec M, Os´cik J, Marczewski AW. Correlations among parameters of Dubinin-Radushkevich and Langmuir-Freundlich isotherms for adsorption from binary liquid mixtures on solids. *Journal of Colloid and Interface Science*. 1987;117(2):339-346.

54. Yao C. Extended improved Langmuir equation for correlating adsorption equilibrium data. *Separation and Purification Technology*. 2000;19(3):237-242.

55. Praus P, Turicová M. A physico-chemical study of the cationic surfactants adsorption on montmorillonite. *Journal of the Brazilian Chemical Society*. 2007;18(2):378-383.

56. Oyetade OA, Skelton AA, Nyamori VO, Jonnalagadda SB, Martincigh BS. Experimental and DFT studies on the selective adsorption of Pb^{2+} and Zn^{2+} from aqueous solution by nitrogen functionalized multiwalled carbon nanotubes. *Separation and Purification Technology*. 2017;188:174-187.

57. Vázquez G, Mosquera O, Freire MS, Antorrena G, González-Álvarez J. Alkaline pre-treatment of waste chestnut shell from a food industry to enhance cadmium, copper, lead and zinc ions removal. *Chemical Engineering Journal*. 2012;184:147-155.